COLORS OF KUIPER BELT OBJECTS: THE RELATIONSHIP BETWEEN KBO COLORS AND KUIPER BELT PLANE INCLINATION

By

Julia Frances Kane

B.S. Mathematics with Computer Science
Massachusetts Institute of Technology, 2004

SUBMITTED TO THE DEPARTMENT OF EARTH, ATMOSPHERIC AND PLANETARY SCIENCES IN PARTIAL FULFILLMENT OF THE REQUIREMENTS FOR THE DEGREE OF

MASTER OF SCIENCE IN EARTH, ATMOSPHERIC AND PLANETARY SCIENCES
AT THE
MASSACHUSETTS INSTITUTE OF TECHNOLOGY

JUNE 2006

Author:____________________________
Department of Earth, Atmospheric and Planetary Sciences
12 May 2006

Certified by:____________________________
James L. Elliot
Professor of Planetary Astronomy and Physics
Thesis Supervisor

Accepted by:____________________________
Maria T. Zuber
E.A. Griswold Professor of Geophysics
Head, Department of Earth, Atmospheric, and Planetary Sciences

COLORS OF KUIPER BELT OBJECTS: THE RELATIONSHIP BETWEEN KBO COLORS AND KUIPER BELT PLANE INCLINATION

By

Julia F. Kane

Submitted to the Department of Earth, Atmospheric and Planetary Sciences on May 12, 2006 in Partial Fulfillment of the Requirements for the Degree of Master of Science in Earth, Atmospheric and Planetary Sciences.

ABSTRACT

A large population of small, icy bodies orbits the sun just beyond Neptune, known as the Kuiper Belt. These objects, thought to be the progenitors of short period comets, could provide a sample of primordial material in our solar system, constraining solar system formation models. The colors of Kuiper belt objects (KBOs) can indicate different surface compositions, environmental conditions, or formation characteristics within the Kuiper Belt. Data from the Deep Ecliptic Survey (DES, Millis et al. 2002) have been used to determine the plane of the Kuiper Belt, identifying "core" and "halo" populations with respect to this plane (Elliot et al. 2005). By comparing the colors of objects as a function of inclination, trends can be established distinguishing the core and halo populations. Sloan g', r', and i' observations were obtained from the 6.5-m Clay telescope at Las Campanas Observatory of 14 KBOs, which were combined with previously published data to examine the transition between these two populations as a function of color. For inclination bins containing equal numbers of KBOs, the percentage of red objects (B–R > 1.56, where B–R = 1.56 is the median of the sample) decreases with increasing inclination in a smooth, but nonlinear fashion. This steady decrease could imply that the objects at lower inclinations are less perturbed than those at higher inclinations, resulting in redder surfaces. Additionally, the objects at lower inclinations could represent a primordial population of objects, available to study and to constrain the formation models of the solar system.

Thesis Supervisor: James L. Elliot

Title: Professor of Planetary Astronomy and Physics

Colors of Kuiper Belt objects

INTRODUCTION[1]

Beyond Neptune, there exists a large population of small, icy bodies known as the Kuiper Belt. Within it, ~70,000 objects having diameters greater than 100 km (Luu and Jewitt 1996b) orbit the sun in the outer reaches of our solar system. An early notion of the Kuiper Belt came from Leonard (1930): "Is it not likely that in Pluto there has come to light the *first* of a *series* of ultra-Neptunian bodies, the remaining members of which still await discovery but which are destined eventually to be detected?" Then, in 1949, while considering theories on the origin of the solar system, Edgeworth stated that he believed that the solar system did not have an abrupt edge just beyond Neptune, rather the mass slowly leveled off as distance from the sun increased. He argued that this region lacked the necessary material to form a planet, instead resulting in many small "clusters" of objects, similar to the asteroid belt. He posited the existence of the a belt of objects, proposing that "[it] is not unreasonable to suppose that this outer region [past Neptune] is now occupied by a large number of comparatively small clusters, and that it is in fact a vast reservoir of potential comets" (Edgeworth 1949). In 1951, Kuiper, also discussing possible solar system formation models, similarly suggested that beyond Neptune the surface density of material was insufficient to form into a planet and so formed into "aggregates" up to 1 km in size. He believed that these bodies were scattered by Pluto (and then more so by Neptune, Saturn and Jupiter), entering the inner solar system as comets (Kuiper 1951).

In 1992, Jewitt & Luu detected the first object, 1992 QB_1, in what is now known as the Kuiper Belt (Jewitt and Luu 1993). Kuiper Belt objects (KBOs) are designated following Minor Planet Center (MPC) naming conventions: the year, followed by a two letter code indicating the portion of the year the object was discovered, followed by a subscript number indicating the order that object was discovered. Since then, more than 1000 KBOs, have been identified through a variety of surveys, resulting in several dynamical groupings, including Classical, Scattered and Resonant objects. This classification scheme has been put into a rigorous

---

[1] Presented to the Planetary Internal Colloquium Series on 5 APRIL 2006

framework by the Deep Ecliptic Survey (DES,Elliot et al. 2005), which integrates the orbits of KBOs for 10 Myr, accounting for the gravitational effects of Neptune, Uranus, Jupiter, and Saturn in addition to that of the Sun. The DES defines the classes as follows:

(i) Resonant objects are objects in mean motion resonances with Neptune. One hundred and seven resonant arguments are tested by the DES for librations, or bounded oscillations. While 31 resonances are tested for membership, only 11 resonances have been populated so far[2], including 1:1, 5:4e, 4:3e, 3:2e, 5:3e^2, 7:4e^3, 9:5e^4, 2:1e, 7:3e^4, 5:2e^3, 3:1e^2 (Elliot et al. 2005).

(ii) Scattered objects are non-resonant, non-planet crossing KBOs that have a Tisserand[3] parameter less than 3 or a Tisserand parameter greater than 3 and an eccentricity greater than 0.2. This grouping is broken up into two sets: Scattered-Near and Scattered-Extended. If the object's time-averaged Tisserand parameter, relative to Neptune, is less than 3, the object is considered to be Scattered-Near. If its time-averaged Tisserand parameter is greater than 3 and its eccentricity is greater than 0.2, it is Scattered-Extended.

(iii) Classical objects are those having time-averaged Tisserand parameters greater than 3 and eccentricities less than 0.2. These objects have relatively circular orbits and are mostly unperturbed by Neptune.

(iv) A final grouping of objects is the objects whose orbital elements are not known well enough to determine any of the above classifications. These objects are not designated and are instead labeled as "ERR2LARGE" by the DES. They require further observations to place them into one of the above classes.

---

[2] Resonances populated as of 11 November 2005

[3] The Tisserand parameter is a benchmark in determining dynamical properties of an object before and after encounters with a solar system body (Neptune, in this case), i.e. whether or not the objects current orbital elements were modified by a close encounter with Neptune. Murray, C. D., and S. F. Dermott 1999. *Solar System Dynamics.* Cambridge University Press, Cambridge.

BACKGROUND

Dynamical Background

The Deep Ecliptic Survey (Millis et al. 2002; Elliot et al. 2005) was a survey designed to cover a large area of sky over the course of several years (1998-2005) to discover and dynamically classify ~500 KBOs. Recent results from the DES find the orbital pole of the Kuiper Belt plane (KBP) to be at a right ascension (RA) of 273.92±0.62° and a declination (Dec) of 66.70±0.20° (inclination 1.56° and ascending node 96.7° relative to the ecliptic, Elliot et al. 2005). This plane is consistent with the invariable plane (RA = 273.9°, Dec = 66.99°), but varies from the ecliptic (RA = 270°, Dec = 66.6°) by several degrees. Using the new plane, new KBO orbital pole positions were calculated and plotted (see Figure 1), revealing two distinct populations with respect to the pole of the Kuiper Belt plane, termed "core" and "halo."

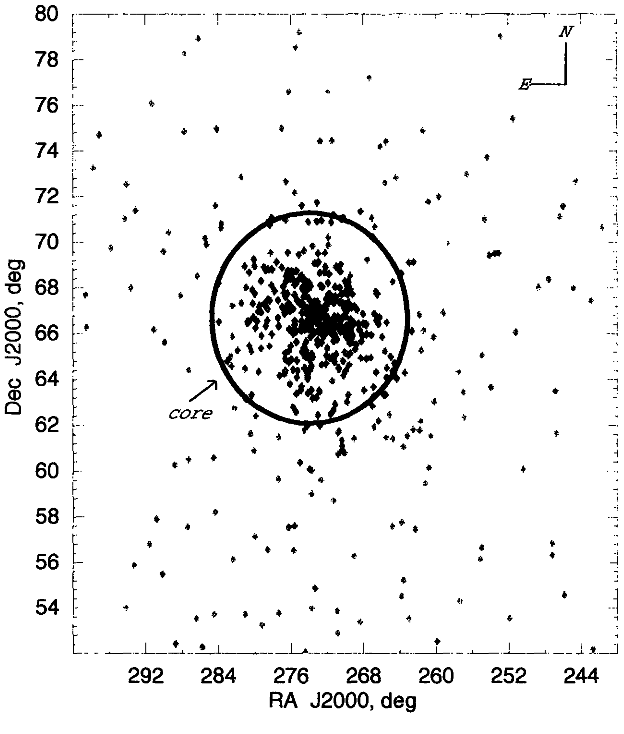

Figure 1: Orbital poles of Kuiper Belt objects. Orbital elements of 552 provisionally designated KBOs were taken from the Lowell Observatory database on Jan 31, 2006. (Buie et al. 2003). The x represents the pole position of the Kuiper Belt plane. The core objects, those with inclinations ≤ 4.6° with respect to the Kuiper Belt plane, are demarked by the black circle. The objects outside the black circle comprise the halo population. (Gulbis et al. 2006)

The core objects are represented by a dense concentration in orbital poles within a few degrees of the pole of the Kuiper Belt plane, while the halo objects have a broad, shallow distribution. Figure 20a from Elliot *et al.* (2005) also shows these two populations as a double-peaked unbiased KBO inclination distribution. Although there is no abrupt boundary, the best fit to the unbiased inclination distribution shows that the core objects are those having inclinations $i_K \leq 4.6°$ with respect to the Kuiper Belt plane, while the halo distribution extends out to $i_K \sim 35°$. Brown first noted this double peak in 2001 (Brown 2001). He fit a double-peaked Gaussian to the distribution of KBO inclinations with respect to the ecliptic plane. The DES followed his example by fitting a double-peaked Gaussian to the data, although they found that a Gaussian plus Lorentzian fit equally well (Figure 20a, Elliot et al. 2005). Note that these fits are somewhat arbitrary choices, aimed at describing the shape of the distribution. There is no particular physical justification to the mathematical functions applied.

Building from the inclination distribution, several Kuiper Belt formation models can be considered. Levison & Stern (2001), speculating on the existence of two distinct, classical ($a >$ 42.5 AU, $e <$ 0.2) populations, defined these two populations in the Kuiper Belt: "hot" (inclinations with respect to the ecliptic greater than 5°) and "cold" (inclinations with respect to the ecliptic less than 5°). They considered the cold population to be a primordial population of objects in the solar system, while the hot population was made up of dynamically perturbed objects. Based on inclination cutoffs, these hot and cold populations are related (but not identical) to the halo and core populations noted by the DES, since these populations both have inclination cutoffs near ~5°. Note that the hot/cold and halo/core populations differ on several levels. First, the hot/cold population inclinations are taken with respect to the ecliptic, while the halo/core population inclinations are taken with respect to the calculated Kuiper Belt plane. The difference in inclinations for any particular object could be as larger as 1.56°. Next, the hot/cold division only considers classical objects, in a non-rigorously determined fashion. In this case, Levinson & Stern (2001) specify $a >$ 42.5 AU, $e <$ 0.2, but other groups using the hot/cold divisions do not specify their classical criteria. The halo/core division does not exclude the

Scattered Disk Objects and bases its classifications on a rigorous classification scheme as specified above.

Another model, building on Levison & Stern (2001), considers different methods by which three sets of objects were incorporated into the Belt (Morbidelli et al. 2003). The first set of objects formed between Jupiter and Uranus and was scattered outward during planetary migration. These objects are now excited (having high inclinations and/or eccentricities) and form a hot population of KBOs. Another set of objects formed in the region of the current Kuiper Belt (~35-50 AU) and has not been dynamically perturbed. These objects form the population of cold KBOs. The final set of objects is the resonant objects – those bodies that now orbit in mean-motion resonance with Neptune. Another formation model possibility is that all of the KBOs formed as low inclination cold objects, but a subset was excited into higher inclinations, constituting the hot population.

Color Background

One way to test formation theories is to look at the physical characteristics of KBOs. If they are physically the same, then it is likely they came from the same original population. If the physical characteristics are not the same, then either alternate processes affected the objects, or the populations are inherently separate. Photometric color observations provide insight into the composition of objects and allow comments on the extent to which environmental conditions such as space-weathering or impact gardening have played a role in the modification of these surfaces. Several groups have investigated colors in the Kuiper Belt.

Luu & Jewitt (1996a) determined the $B–R$ colors of 9 KBOs. They found that the colors spanned a large range, from solar-like to very red, and that the color distribution of the KBOs was not statistically different from that of the comets. Since then, other color work has been done by a variety of groups. These include Green et al. (1997), Jewitt & Luu (1998), Tegler & Romanishin (1998), Barucci et al. (1999), Davies et al. (2000), Tegler & Romanishin (2000), Barucci et al. (2001), Doressoundiram et al. (2001), Boehnhardt et al. (2001), Jewitt & Luu

(2001), Doressoundiram et al. (2002), Tegler et al. (2003), Delsanti et al. (2004), Peixinho et al. (2004) and Gulbis et al. (2006).

Tegler & Romanishin (1998) noted the first KBO color correlation. Presenting photometry for 11 objects and using 13 objects in their sample, a color-color plot showed two distinct populations of objects: approximately solar-colored and extremely red. They suggested that cometary activity, such as coma formation, might result in the neutral colors seen in the Kuiper Belt (Tegler and Romanishin 1998).

Doressoundiram et al. (2001) suggested that objects with higher inclinations were less red than objects at low inclinations, even though Jewitt & Luu (2001) explicitly state that there is no correlation expected between color and inclination. Then, in 2002, Trujillo & Brown (2002) found a linear correlation between orbital inclination and B–R colors of non-Resonant KBOs; $B-R = (-0.0196 \pm 0.003)i + 1.84 \pm 0.5$ (Figure 1, Trujillo and Brown 2002). They showed that as non-Resonant object inclinations increase, the KBOs become less red.

The largest contribution to determining colors of KBOs is the Meudon Multicolor Survey of Outer Solar System Objects (2MS), started in 1997 (Doressoundiram et al. 2002). Using the divisions of hot and cold populations as defined by Levison & Stern (2001) and considering the classical population (semimajor axes between 40 and 48 AU), they note color differences between these two groupings. The cold objects tend to be red while the hot objects have more varied colors. Tegler et al. (2003) confirm these results, claiming that small inclination & eccentricity objects are primarily red, while large inclination and eccentricity objects tend to be more neutral.

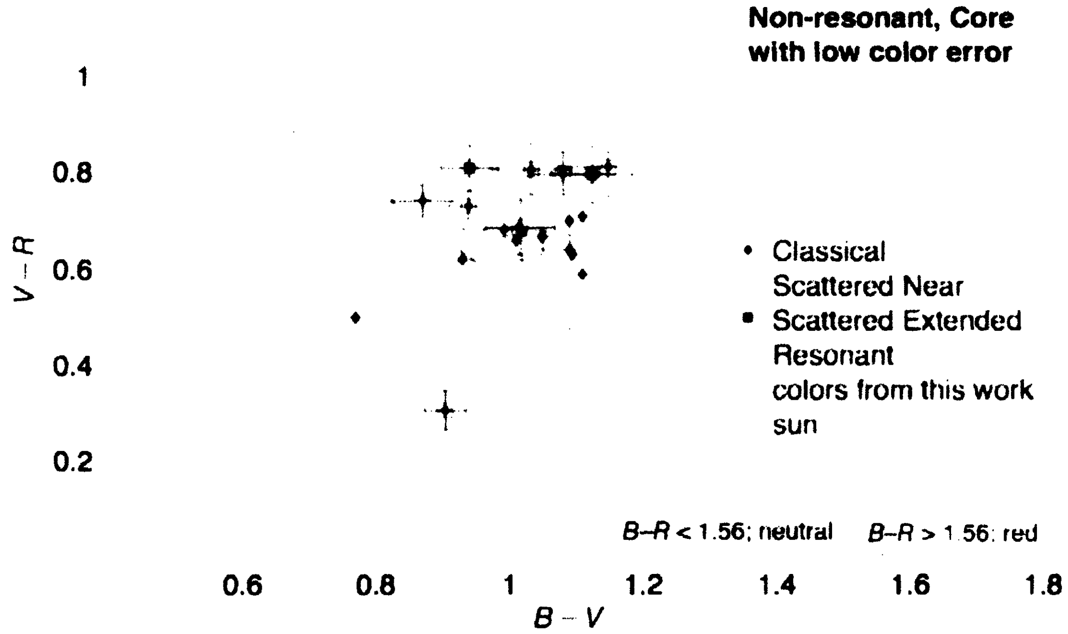

Figure 2: Color-color plot of core KBOs (i_K < 4.6°): adapted from Figure 3 from Gulbis et al (2006). This plot shows the colors of non-resonant objects in the core; with color error bars less than 0.1 mag. It is clear looking at this plot that there is a cluster of red objects in the core with a few outliers that could be objects from the halo population. (Gulbis et al. 2006).

Gulbis et al. (2006) studied the colors of the core Kuiper Belt objects (those having inclination with respect to the Kuiper Belt plane $i_k \leq 4.6°$), finding them to be primarily red, unlike the halo objects which have colors ranging from red to neutral. This result is similar to that of Peixinho et al. (2004) who show the cold population is primarily red when the inclination cutoff is set at 4.5° (with respect to the ecliptic plane), further refining the results of Levison & Stern (2001). Gulbis et al. (2006) also found that although the resonant population as a whole is diverse, when broken down into specific resonances, the groupings each have trends (diverse, very red, or very neutral).

The observation that the core is red leads to the question of what happens outside of the core and whether there is a distinct boundary between the core and halo populations. A first step to understanding this transition is to determine the nature of the transition. The Minor Bodies of the Outer Solar System database (MBOSS; (http://www.sc.eso.org/~ohainaut/MBOSS, Hainaut and Delsanti 2002) was used to study the colors of KBOs within several zones surrounding the core. The MBOSS database contains *B–V* and *V–R* colors for KBOs and Centaurs, compiled from all published colors as of September 2005. Colors of objects in the transition zone between the core and the halo are not well determined due to lack of data. To remedy this issue, more KBOs were observed on the Clay 6.5-m Magellan Telescope at Las Campanas Observatory.

OBSERVATIONS

This work focuses on observations of objects in several inclination zones centered at the pole of the Kuiper Belt in order to determine trends in the colors of these KBOs. For the initial look at the data, KBOs with inclination errors less than 0.05° were chosen from the Lowell database as of September 1, 2004. In order to determine where more data would be needed, data were taken from the June 4, 2003 version of the MBOSS database and divided into six preliminary inclination bins, two in the core ($i_k \leq 4.6°$) and four outside the core ($i_k > 4.6°$). From Table 1, it is clear that more data are needed in several of the bins in order to understand trends with any statistical significance.

TABLE 1: KBO STATISTICS, BINNED BY INCLINATION WITH RESPECT TO THE KUIPER BELT PLANE. NOTE THAT FOR THIS DATASET RED IS DEFINED AS *B–R* > 1.5[A]

KBP inc. range (i_k)	Total no. KBOs[B]	Resonant			Non-Resonant			
		No. colors[B]	Red KBOs	Neutral KBOs	No. colors[B]	Red KBOs	Neutral KBOs	Fraction red
0°-2.3°	190	5	3	2	30	25	5	0.83
2.3°-4.6°	107	3	2	1	10	10	0	1.00
4.6°-9°	88	14	7	7	10	6	4	0.60
9°-17°	89	11	7	4	12	8	4	0.67
17°-26°	53	3	1	2	17	5	12	0.19
26°-35°	22	0	0	0	9	2	7	0.22

[A] Note that the inclination cutoff was chosen generally for the first look and refined to 1.56 later in this work. The two bins above the bold line represent the core. The four bins below the bold line represent the halo.

[B] The total number of KBOs was determined from the Lowell database on September 1, 2004. The number of colors for resonant and non-resonant KBOs was determined from the MBOSS database as of June 4, 2003 as being objects with both *B–V* and *V–R* colors.

Proposal Planning, Target Selection

Time on the Magellan Telescopes was requested to observe KBOs distributed among the less populated bins listed in Table 1.

The multi-color observations of KBOs are best performed using the Raymond and Beverly Sackler Magellan Instant Camera (MagIC,Osip et al. 2004) on the Clay telescope. This instrument, built at MIT, has a SITe 2048 x 2048 pixel quad-amp CCD camera with a 0.069 arcsec/pixel plate scale. MagIC has the high sensitivity, resolution, and filters to perform color photometry observations.

Each object was exposed for a ten-exposure sequence in Sloan (g', r', and i') filters because they are more discerning in color differences than the Johnson-Cousins system, they eliminate the strongest night-sky lines, and the colors do not overlap. Additionally, since the bandpasses are wider than the standard Johnson-Cousin system, these filters are ideal for detecting faint objects like KBOs. Data obtained using Sloan filters can then be transformed to Johnson-Cousins filter colors for comparison (Smith et al. 2002).

The objects chosen for observation cover a range of inclinations and dynamical classifications. Table 2 presents the objects observed in order of increasing KBP inclination, providing inclination with respect to the ecliptic for comparison. The table also provides the values for eccentricity, semi-major axis and perihelion for each of the observed KBOs, as determined on January 31, 2006 by the Lowell Observatory database (Buie et al. 2003).

The exposure sequence was planned to achieve a maximum magnitude error of 0.05 mag. Exposure times were calculated starting with previous data taken in a predecessor observing program (Gulbis et al. 2006) and then extrapolating appropriate exposure times (Elliot, personal communication). The previous data were used to set reference values for signal-to-noise ratio $\mathrm{SNR}_{\mathrm{ref}}$, seeing θ_{ref}, sky background $a_{\mathrm{sky,ref}}$ and exposure time Δt_{ref}. These values were then used to determine a reference magnitude $\mathrm{m}_{\mathrm{ref}}$, from which an exposure time could be determined:

$$\Delta t = \Delta t_{\mathrm{ref}} \left(\frac{\mathrm{SNR}_{\mathrm{obs}}}{\mathrm{SNR}_{\mathrm{ref}}}\right)^2 \left(\frac{\theta_{\mathrm{FWHM}}}{\theta_{\mathrm{FWHM,ref}}}\right)^2 \left(\frac{a_{\mathrm{sky}}}{a_{\mathrm{sky,ref}}}\right) 10^{+0.8\left(m_{\mathrm{obj}} - m_{\mathrm{ref}}\right)}. \tag{1}$$

TABLE 2: KUIPER BELT OBJECTS OBSERVED (IN ORDER OF INCREASING KBP INCLINATION).

Object	Class^a	i_K (deg)^b	i (deg)^c	e^c	a (AU)^c	q (AU)^c	Obs. Filter Sequence	Exp. Time (sec)^e		
								g'	r'	i'
2002CC$_{249}$^{d2}	CL	$2.33\pm^{0.27}_{0.27}$	0.84	0.20	47.4	38.0	$2r'$-$3i'$-$3g'$-$2r'$	120	120	120
2000CN$_{105}$^{d3}	CL	$3.16\pm^{0.26}_{0.20}$	3.41	0.09	44.7	40.5	$2r'$-$3i'$-$3g'$-$2r'$	60	60	60
2001KN$_{76}$^{d3}	7:4e^3	$3.84\pm^{0.31}_{0.30}$	2.64	0.09	44.0	39.9	$2r'$-$3i'$-$3g'$-$2r'$	60	60	60
2000QL$_{251}$^{d3}	2:1e	$4.78\pm^{0.32}_{0.30}$	3.68	0.21	47.6	37.4	$2r'$-$3i'$-$3g'$-$2r'$	60	60	60
119066^{d3}	7:4e^3	$5.82\pm^{0.27}_{0.31}$	6.72	0.08	43.9	40.4	$2r'$-$3i'$-$3g'$-$2r'$	180	120	60
2002KW$_{14}$^{d1}	CL	$8.55\pm^{0.30}_{0.32}$	9.75	0.20	47.0	37.4	$2r'$-$3i'$-$3g'$-$2r'$	60	60	60
120132^{d1}	SE	$12.50\pm^{0.32}_{0.28}$	11.76	0.26	49.8	37.1	$2r'$-$3i'$-$3g'$-$2r'$	120	120	120
2002GJ$_{32}$^{d1}	CL	$12.94\pm^{0.31}_{0.30}$	11.59	0.11	44.5	39.7	$2r'$-$3i'$-$3g'$-$2r'$	60	60	60
2001HY$_{65}$^{d2}	SN	$17.20\pm^{0.26}_{0.20}$	17.10	0.12	43.5	38.1	$2r'$-$3i'$-$3g'$-$2r'$	120	120	120
2002MS$_4$^{d4}	SN	$18.48\pm^{0.32}_{0.28}$	17.67	0.14	41.9	36.0	$2r'$-$3i'$-$3g'$-$2r'$	60	60	60
2001KO$_{77}$^{d3}	SN	$22.04\pm^{0.31}_{0.30}$	20.69	0.15	44.2	37.5	$2r'$-$3i'$-$3g'$-$2r'$	60	60	60
90568^{d1}	SN	$23.37\pm^{0.30}_{0.30}$	21.95	0.08	42.3	38.8	$2r'$-$3i'$-$3g'$-$2r'$	60	60	60
2002GH$_{32}$^{d1}	SN	$27.51\pm^{0.32}_{0.29}$	26.61	0.09	42.3	38.5	$4r'$-$6i'$-$6g'$-$4r'$	60	60	60
120216^{d4}	3:2e	$28.75\pm^{0.23}_{0.29}$	29.23	0.32	39.7	27.0	$2r'$-$3i'$-$3g'$-$2r'$	60	60	60

[a] Dynamical classifications are based on the system described in Elliot et al. (2005): Classical – CL, Scattered Extended – SE, Scattered Near – SN, Resonant –(3:2*e*, 2:1*e*, and 7:4*e*^{3}).

[b] Errors in inclination with respect to the Kuiper Belt plane are dominated by the error in the measured pole of the plane (as listed in Table 13, Elliot et al. 2005).

[c] Orbital elements are from the Lowell Observatory database (Buie et al. 2003) on 31 Jan 2006. The errors on i (ecliptic inclination), e (eccentricity), a (semi-major axis), and q (perihelion) are smaller than the least significant digit.

[d] Observation date key: 1 – 14 April, 2005, 2 – 15 April 2005, 3 – 7 June 2005, 4 – 8 June, 2005.

[e] Magnitude ranges for exposure times, assuming seeing < 0.7'': $m_v < 20.5$: 60s-60s-60s; $20.5 < m_v < 21.5$: 120s-120s-120s; $m_v > 21.5$:180s-120s-60s. As the seeing increased, exposure times were increased accordingly.

Assuming a 22.2 *V*-mag KBO at the zenith, no Moon, and a median seeing of 0.7", we required four frames of 120 sec in r', three frames of 180 sec in g', and three frames of 60 sec in i'. The resulting integration time is approximately 20 min per object. Allowing 25 seconds readout time per frame, 20 seconds for each filter change, and 2 minutes overhead between objects, the total time required for observing an object was approximately 27 minutes. Observing standard stars required 15 additional minutes each night. Three images of a standard star were taken in each filter at a variety of airmasses throughout the night. Due to the faintness of the targets (with *V* magnitudes as faint as 22.9), dark time was important for these observations. Sky darkness and good seeing could both be slightly sacrificed, but at the expense of integration time. To illustrate the importance of dark sky and good seeing conditions, consider the integration times as the seeing goes up to 1.0" with the same conditions listed above. The total integration time per object nearly doubles to 48 minutes.

Observation Strategy

Data were acquired from two runs on four nights, April 14-15, 2005 and June 6-7, 2005, observing the objects in 3 different Sloan filters (g', i', r') on MagIC, following the same sequence ($2r'$-$3i'$-$3g'$-$2r'$). Bright objects were chosen to guarantee that all exposure times were less than 120 seconds. Short exposure times ensured objects did not trail significantly during the exposure. Typical KBOs move at a maximum rate of approximately 3''/hr at opposition: in 180 seconds, the object will move ~0.15''. Since even the best seeing at LCO is only slightly better than ~0.3'', for this exposure time the KBOs will not appear trailed on the image and can be assumed to the circular and share a PSF with the on-chip stars, a condition required for aperture correction photometry. Additionally, signal-to-noise ratios of ~25 were desired in order to keep the error bars less than 0.05 mag. When the seeing got worse, the number of exposures was doubled to allow increasing SNR by stacking frames. Standard stars were taken throughout the night to cover a wide range of airmasses (ideally 1.1 – 1.8). Observations of 24 KBOs were taken over the course of the observing runs. Due to bad weather (clouds, bad seeing), the data for 10 of these objects were not reducible. Table 2 lists all the dynamical and observation information for the successfully observed objects. Three of these objects have published color indices, in order to provide a consistency check.

PHOTOMETRIC REDUCTION

All photometry was performed using IRAF, an “Image Reduction and Analysis Facility” that is designed to process images. Specifications for reducing MagIC images using IRAF were found at http://www.lco.cl/lco/magellan/instruments/MAGIC/iraf_reductions.html.

Calibrations

First, the frames were calibrated using the MagIC package written for IRAF. The MAGIC_GAIN script outputs the gain and read noise, so that the user can verify these quantities are sufficiently low and constant. Values on all four observing nights were consistently ~6 for the read noise and ~2 for the gain.

Next, the CCDMAGIC routine, written by Nick Suntzeff, subtracts the bias (as computed by averaging the overscan region for that quadrant) and removes the overscan regions from the image. The bias level corresponds to the offset inherent in the detector for a 0-second exposure. Removing the bias is necessary to ensure that there is no underlying structure from the detector in the image.

Another source of noise that is typically calibrated out of images is the dark current level. A “dark” frame is normalized to the same exposure time as the image it is used to calibrate, except that the shutter remains closed. This calibration removes any thermal levels that grow linearly in the detector with time. Previous work in the group (Figure 8, Kern 2005) has shown that, for MagIC, the dark current level and dark current noise (~0.5±0.1 ADU; for exposure times up to 1200 sec) are negligible and so this reduction step is not necessary.

Finally, the pixel-to-pixel variations in the CCD were removed by dividing each image by a normalized flat field frame. For each observing run, a set of flat fields (one for each filter used) was created using the FLATCOMBINE routine in IRAF. This routine combines all the flat images in a particular filter for a given observing run and then scales them by the inverse of the mode. The mode is chosen since it represents the maximum-likelihood estimator for the data in that region (Stetson 1987). After each data frame is divided by its corresponding flat field, a calibrated frame is produced.

Locating Objects

Once the data frames were calibrated, the next step was to locate the faint KBOs. The first and last frames of each KBO sequence were opened in the IDL procedure, "Looker", written by Marc Buie (Millis et al. 2002). Looker was designed for the Deep Ecliptic Survey to aid in searching for moving objects. The two frames are read into different color planes (red and cyan respectively) and then overlaid. Stationary objects appear white, but moving objects appear as red-cyan pairs. In most cases, the objects were moving quickly enough to be easily locatable in this manner. However, for a few of the KBO observations, during the ranges of bad seeing and/or clouds, the objects were un-detectable.

Aperture Correction Photometry

After locating the object, aperture correction photometry, using the PHOT function in the IRAF package APPHOT, was performed on each frame, providing instrumental magnitudes. Aperture correction photometry optimizes the photometry for faint objects, like KBOs. A photometry study of bright and faint objects (Howell 1989) demonstrated that standard photometry techniques for sky removal does not work for faint objects, as the background is often over estimated and the object actually becomes "fainter" with increasing aperture radius (instead of approaching a limit, as bright sources do; see Figure 3). To calculate the magnitude of faint sources, Howell (1989) suggested using a scaling method that applied a "growth curve" correction between bright and faint sources, where the growth curve indicates how the flux from the object "grows" with increasing aperture size. This method uses only high SNR pixels and excludes as many background dominated pixels as possible, decreasing the error in the measurement. Figure 4 shows that the KBOs observed in this project are faint enough to require this correction and also provides a first order estimate of the background error.

To complete the photometry and achieve instrumental magnitudes, IRAF's APPHOT method was used (Davis 1987).

Note that there are several APPHOT assumptions:

- Image data are linear.

- Image data have been calibrated – *i.e.*, data already corrected for cosmic rays, bias level variations, etc.
- Sky background is flat in the general area of the object.
- Point-spread function (PSF) is constant throughout the image.

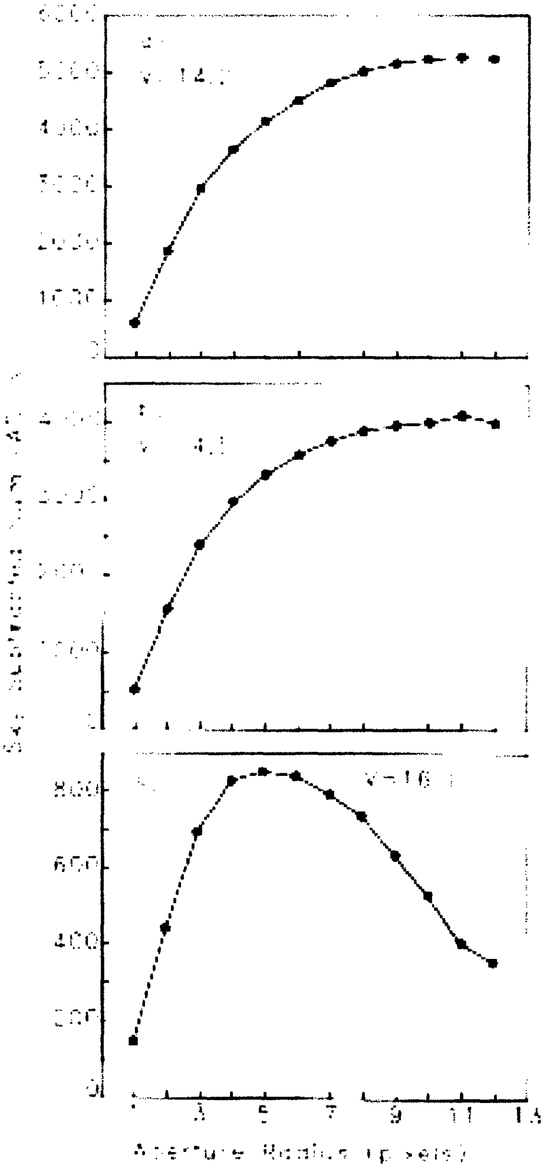

Figure 3: Growth curves for three simulated point sources: Figure 2 from Howell 1989. Each plot shows the sky subtracted counts as a function of radius for three point sources, decreasing in brightness; c) is sky limited. As the objects decrease in brightness, one notices that standard photometry techniques result in the object appearing fainter with increasing aperture radius. Since standard methods fail in the faint object limit, a modified scaling method (aperture correction photometry) that avoids this problem is necessary (Howell 1989).

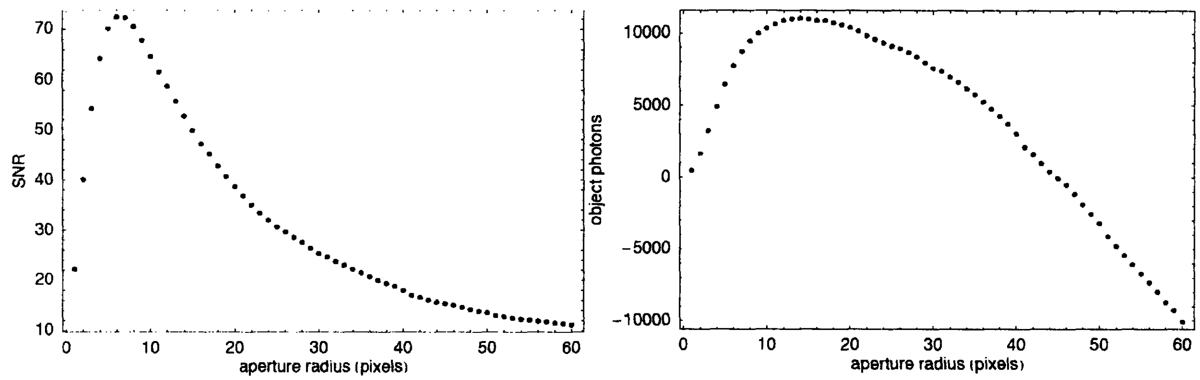

Figure 4: Signal-to-noise ratio (left panel) and DN from photometry (right panel) of 2004EW$_{95}$ (20050608.062.fits) vs. aperture radius in pixels. Left panel: SNR ratios from real data. The optimum aperture radius for this object on this night occurs at 6 pixels, approximately equal to the FWHM for this object of 12 pixels, in agreement with (Romon-Martin 1999). Right panel: Values for object photons are taken using standard photometry methods from IRAF's APPHOT routine and are background subtracted. As the aperture size increases and more light is included, the number of photons from the star should approach a limit. However, for faint objects, the error in the background level can result in the object appearing to become *fainter* with increasing radius. From this plot, it is clear that KBOs require the use of aperture correction photometry to properly determine the magnitude of these objects.

The flux was measured from several bright on-frame stars in both a small and large aperture. The flux from the KBO was measured using only the small aperture. The small aperture was chosen to be a few pixels greater than the FWHM (full-width at half-maximum) of the KBOs for a given night of observing, since this choice maximizes the signal-to-noise (Romon-Martin 1999)[4] and avoids any edge effects of choosing an aperture equal to the FWHM. Looking at Figure 4, we see that the optimum aperture does agree with the work of Romon-Martin. The aperture radius of 6 pixels optimizes SNR and is approximately equal to the FWHM of that particular object, 12 pixels. It is important to note that a first order approximation of the error is given by 1/SNR. For a more detailed treatment on the computation of the SNR, see the section on *Error Analysis*. The large aperture was chosen to be three times the largest FWHM of the standard stars, ensuring that as much of the light as possible from these brighter objects was included in the aperture. Assuming an Lorentzian PSF of the form:

$$PSF(r) = \frac{1}{1+r^3}, \tag{2}$$

---

[4] Romon 1999 is a Master's thesis from University of Paris. I was unable to obtain a copy of the document to fully understand the process Romon used to determine the optimum choice of FWHM.

and integrating $PSF(r) \cdot r \cdot dr$ from $r = 0$ to r = 6*r_H, where r_H = FWHM/2 we note that 86% of the light is included in the aperture.

PHOT also removes the sky background from the aperture. The sky background is computed as an annulus around the object (with an inner annulus of 4 times the FWHM of the standard stars pixels and an outer annulus 10 pixels larger). Note that IRAF uses partial pixels for photometry when necessary. The fitting routine accounts for the possibility of faint stars or galaxies in the annulus when determining the sky background and removes them by performing an iterative removal of any pixel that is more than 3-sigma from the mode[5] of the background sample. Specific values used during the reduction can be found in Table 2.

The small aperture decreases the error due to sky background noise, but also removes some of the flux from the KBO that would be included with a larger radius. To account for this discrepancy, the ratios of the two apertures for the on-frame stars are averaged to compute an aperture correction factor for that frame. This ratio is then applied to the KBO to account for the lost object light, while avoiding the addition of more background signal (Barucci et al. 2000). In order for this method to be applicable, the PSF of the faint object must have the same shape as the on-frame stars. The fastest moving KBO observed (2001KO$_{77}$) moved at a rate of 3.28''/hour. The longest exposure for that KBO (which was also the longest exposure for all the KBOs) was a 180 second exposure in *g'*. Given the 0.069''/pixel scale of MagIC, these values imply that the KBO moved 2.38 pixels over the course of the exposure. Given that the smallest aperture used was 8 pixels, it is valid to assume that the PSF of the KBO has the same shape as the on-frame comparison stars. Numerical simulations comparing a moving circular Lorentzian PSF and a stationary one agree within the 3-sigma level. Additionally, when comparing the amount of light lost by assuming a moving object is stationary, we find that only 0.6% of the light is not included. While modeling PSFs will remove this error and slightly improve the results, the approximation also works well.

---

[5] Note that "mode" refers to IRAF's definition of mode, which is $I_{\mathrm{mode}} = 3.0 * I_{median} - 2.0 * I_{mean}$. This definition holds for unimodal curves with moderate asymmetry.

TABLE 2: IRAF SETTINGS USED FOR EACH NIGHT OF DATA REDUCTION[a]

Obs. Date (UT)	FWHM PSF[b]		Background Sigma		Background Annulus Inner Radius[c]	Photometry Apertures
	Standard	KBO	Standard	KBO		
April 14, 2005	17	17	5	7	72	19, 51
April 15, 2005	14	13	6	8	60	15, 45
June 7, 2005	20	13	5	10	80	15, 60
June 8, 2005	15	12	5	5	60	14, 45
July 10, 2005[d]	13	no KBOs observed	4	no KBOs observed	56	15, 42

[a] All of the above values are in units of pixels.

[b] When choosing the FWHM PSF for a given night of observation, the largest FWHM on an individual frame was used on all frames. Standard refers to all standard star frames, while KBO refers to all frames containing a KBO. The KBO FWHM is chosen from on-chip comparison stars.

[c] The value of the outer radius is 10 pixels larger than that of the inner radius.

[d] No KBOs were observed on this night because it was used to create a transfer network for April 15, 2005, since there were not adequate standard stars for that night.

Standard Stars

Standard stars were taken at a range of airmasses throughout the night and were used to calibrate magnitudes. Standard stars were chosen from the Sloan Digital Sky Survey (SDSS,Smith et al. 2002), through a survey project undertaken by the US Naval Observatory (USNO) in Flagstaff, AZ to provide photometric calibrations for the SDSS. First, the list was culled to choose objects of an appropriate magnitude for the 6.5-m Magellan Telescopes (~12-14 magnitude) to avoid saturation. Then, plotting a wide range of standard stars on a $B-V$ vs. $V-R$ plot, stars with similar colors to the KBOs were chosen. Those objects with colors in the same range as the observed KBO colors were selected out as possible standard star candidates. Finally, positions in the sky during a particular observing run decided the final set of stars to be used. Stars needed to cover a range of airmass (from 1.0-1.8) throughout the night in order to provide robust extinction curves.

Aperture photometry was also performed on the standard stars to obtain extinction curves for each night of observation. In some cases, the standard stars were saturated due to the seeing being very good and the standard star being too bright. These stars were removed from the calibration pool. Using *Mathematica*, extinction coefficients (*k*) and offsets (*m*) were computed for each night of observation. Sample extinction curves are show in Figure 5. These standard stars allowed the conversion of the instrumental magnitudes obtained through IRAF to magnitudes.

One night, April 15, 2005, lacked adequate standard stars due to sporadic non-photometric conditions. To avoid losing all the data from this night, field stars in the frames for the two KBOs were calibrated on a later observing run, July 9-10, 2005. Magnitudes for the on-frame stars were determined using standard stars taken on that night. Then, the frames from April 15, 2005 were calibrated using the magnitudes determined on July 9-10, 2005. This method allowed the determination of the magnitudes for the KBOs even though there were no

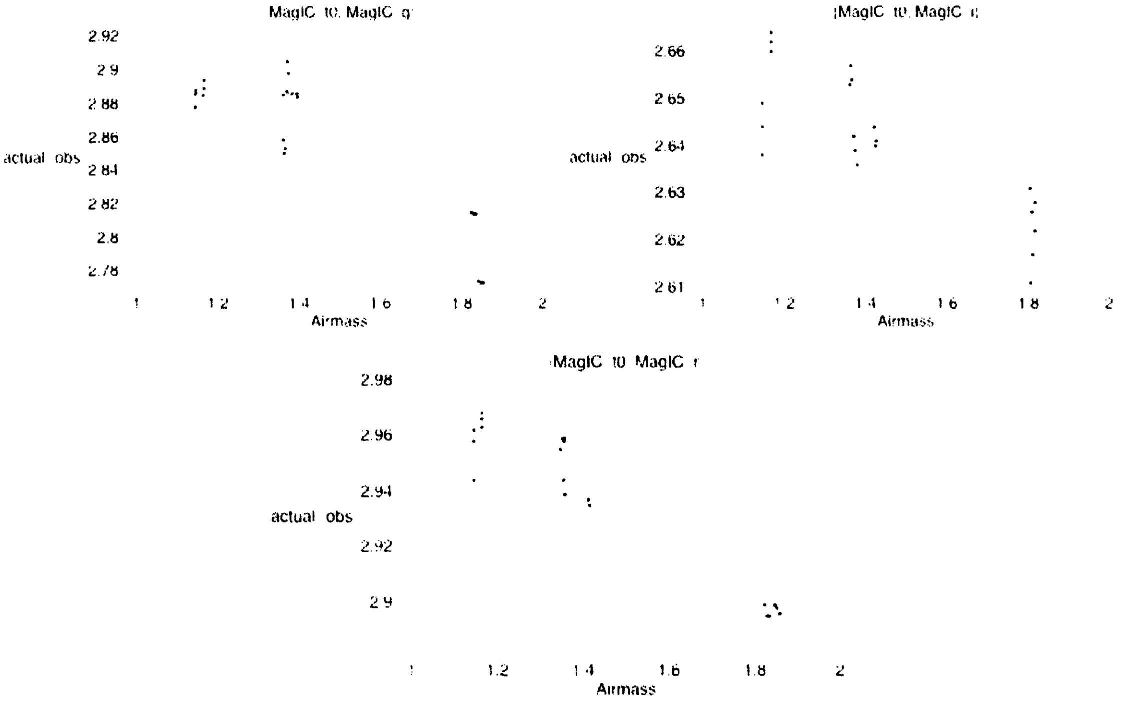

Figure 5: Sample extinction curves for each of the g', i' and r' filters on June 7, 2005. Actual magnitude minus the observed magnitude is plotted versus airmass for each filter. The line of best fit is then used to determine the extinction curve. On this particular night, the extinction coefficients, were $k = -0.14\pm0.02$ for g', $k = -0.05\pm0.01$ for i', and $k = -0.10\pm0.01$ for r'. Separate extinction curves were made for each filter, each night of observation to verify photometric conditions and correct for extinction when converting from instrumental magnitudes to magnitudes.

extinction curves available for that night. The magnitudes for the observed KBOs, along with errors and signal-to-noise ratios (SNRs), are listed in Table 3.

COLOR MEASUREMENTS

Since most published work discusses colors in the Johnson-Cousin color framework, converting to this framework allowed the combination of these results with other works and created a larger database of KBOs with colors. In particular, g', r', and i' colors were converted to $B-V$ and $V-R$ indices.

TABLE 3: SLOAN COLORS AND SNRS OF OBSERVED KUIPER BELT OBJECTS

Object	Avg. SNR per frame			g'	i'	r'
	g'	i'	r'	(mag)[a]	(mag)[a]	(mag)[a]
90568	71	109	121	20.6±0.01	19.5±0.01	19.8±0.005
119066	12	9	15	23.9±0.05	22.5±0.07	23.0±0.04
120132	69	91	106	21.2±0.01	20.1±0.01	20.5±0.01
120216	62	53	69	21.4±0.01	20.6±0.01	20.9±0.01
2000CN$_{105}$	13	14	19	22.7±0.05	21.5±0.04	21.9±0.03
2000QL$_{251}$	9	7	12	23.1±0.07	22.2±0.09	22.4±0.05
2001HY$_{65}$	17	24	25	23.1±0.04	22.3±0.06	22.4±0.06
2001KN$_{76}$	8	12	12	23.7±0.08	22.2±0.05	22.9±0.05
2001KO$_{77}$	15	7	11	23.7±0.04	22.8±0.09	23.4±0.05
2002CC$_{249}$	15	21	24	22.9±0.05	22.2±0.06	22.4±0.06
2002GH$_{32}$	7	12	11	23.2±0.07	21.8±0.04	22.5±0.04
2002GJ$_{32}$	8	8	11	22.9±0.08	22.3±0.08	22.4±0.05
2002KW$_{14}$	12	26	22	22.6±0.05	21.0±0.03	21.7±0.02
2002MS$_{4}$	88	82	106	20.7±0.01	20.1±0.01	20.2±0.01

[a] Errors are determined as explained in the next section.

The Sloan colors were converted to $B-V$ and $R-I$ using Equation 2, following Smith et al. (2002).

$$B-V = 1.02(g'-r') + 0.20$$

$$R-I = \begin{cases} 1.00(r'-i') + 0.21, & r'-i' < 0.95 \\ 0.70(r'-i') + 0.49, & r'-i' \geq 0.95 \end{cases} \quad . \qquad (3)$$

While Smith et al. (2002) does provide color conversions to *V–R* as well, these color relations only depend on the g' and r' Sloan measurements. Therefore, the *R–I* conversion as an intermediary step maintained independence in these results.

Next, the polynomial relation of Caldwell et al. (1993) was used to convert *R–I* to *V–R*. Caldwell et al. (1993) based their relations on photometry done at the South African Astronomical Observatory, in order to provide predictions of color magnitudes in other filters to aid in observational planning:

$$V-R(x)=-0.06+0.34(x-1)+0.13(x-1)^2+1.30(x-1)^3-3.40(x-1)^4-1.30(x-1)^5+9.80(x-1)^6$$
$$+0.78(x-1)^7-11.76(x-1)^8-0.42(x-1)^9+6.44(x-1)^{10}+0.13(x-1)^{11}-1.33(x-1)^{12}+1;$$
$$x=R-I. \tag{4}$$

While these relations are not perfect since they were derived from stellar data, they are the best that are currently available. Data have been taken to create transformations from KBO observations.

Error Analysis

IRAF defines A_{obj} as the total number of counts in the aperture over time Δt, subtracting sky, M_{aper} as the area of the aperture (in pixels), σ_{sky} as the standard deviation of the sky and A_{sky} as the number of sky pixels; zmag is user input and g represents the gain in the CCD electronics (for MagIC, *zmag* is 24.0 and g is 2.0). IRAF errors include the error from the sky noise in the aperture, photon noise error and error of the sky background. The instrumental magnitude and error provided by IRAF are:

$$m_i = zmag - 2.5\log(A_{obj}) + 2.5\log(\Delta t),$$

$$\sigma_{mi} = 1.0857 * \frac{\sqrt{\frac{A_{obj}}{g} + M_{aper}\sigma_{sky}^2 + M_{aper}^2\frac{\sigma_{sky}^2}{A_{sky}}}}{A_{obj}}. \tag{5}$$

Finally, the error in the calibrated magnitude was calculated by propagating the instrumental error and including the error in the standard stars. In this case, taking σ_{mi} as the error in the instrumental magnitude provided by IRAF, σ_k and σ_m as the errors in the slope and intercept of the extinction coefficient calculation from the standard stars, ρ is the correlation coefficient between k and m, and X as the airmass, then the error in the magnitude is:

$$\sigma_{mag} = \sqrt{\sigma_{mi}^2 + \sigma_m^2 + X^2\sigma_k^2 + 2\rho X\sigma_m\sigma_k}\,. \tag{6}$$

It is important to note that the SNR for these objects are determined using $SNR = \dfrac{1.0857}{\sigma_{mi}}$.

There are many other sources of error, including the error in accurately determining the centroid of the object (< 10^{-6}), the error in the aperture ratio (< 10^{-6}), the errors in the standard star magnitudes (< 0.003) and the errors due to scintillation noise, read noise and the dark current noise. However, all of these error factors are negligible compared to the other error terms, especially given the limit of using a large telescope for faint object photometry. In particular, scintillation noise can be approximated using the following equation from Young (1974):

$$\left[\frac{\sigma(s)}{s}\right]_{scin.} = 0.045\left(\frac{1.0cm}{D}\right)^{2/3} * \left(\frac{1.0\sec}{\Delta t}\right)^{1/2} X^2 e^{-h/H}, \tag{7}$$

where D is the diameter of the telescope in centimeters (650 cm), Δt is the exposure time (~60 sec), X is the airmass of the observation (~1.5), h is the altitude of the observatory (2.444 km), and H is the scale height of the atmosphere (~8.4 km). Using the values specified in parentheses (common values for the KBO color observations at LCO), the normalized rms variation is ~$1.30\text{x}10^{-4}$, which translates to approximately 1 photon, using a typical KBO signal total of 3000 photons. Another source of noise, the read noise, ~6 e^-/pixel, corresponds to a read noise variance of 36, which is equivalent to 36 photons/pixel. Given that a typical sky level in 120-second frame is 150 DN/pixel and the gain is 2 e^-/DN, the sky value is ~300 photons/pixel. This background level implies that the read noise results in a 6% increase in the value of the error bar. Finally, the sky level of 300 photons is much greater than the dark current level of ~1 photon/pixel, resulting in a negligible contribution to the error from the dark current variation.

Color Results

The results of the color photometry conversion and errors are listed in Table 4. The r' frames were taken at the beginning and end of each sequence to average any possible color variation and detect any anomalous color values. For the objects with previously measured colors, Peixinho et al. (2004) found $V\text{–}R = 0.67\pm0.13$ for $2000CN_{105}$ and Doressoundiram et al. (2005) found $B\text{–}R = 1.48\pm0.23$ for $2002GH_{32}$ and $B\text{–}R = 1.50\pm0.19$ for $2002GJ_{32}$. These color indices for $2000CN_{105}$ and $2002GH_{32}$ agree within the error bars with the values reported in this work, but $2002GJ_{32}$ disagrees by 0.38 mag.

TABLE 4: JOHNSON-COUSIN COLOR INDICES OF THE KBOS WITH MEASURED COLORS FROM THIS WORK

Object	$B\text{–}V$ (mag)	$V\text{–}R$ (mag)	$B\text{–}R$ (mag)
90568	1.02±0.01	0.62±0.01	1.64±0.01
119066	1.15±0.07	0.83±0.08	1.98±0.09
120132	0.97±0.01	0.63±0.01	1.60±0.01
120216	0.74±0.01	0.58±0.02	1.32±0.02
$2000CN_{105}$[a]	0.96±0.05	0.73±0.05	1.69±0.07
$2000QL_{251}$	0.93±0.08	0.48±0.10	1.41±0.12
$2001HY_{65}$	0.85±0.07	0.38±0.09	1.23±0.10
$2001KN_{76}$	1.11±0.09	0.90±0.07	2.01±0.11
$2001KO_{77}$	0.50±0.06	0.82±0.10	1.33±0.12
$2002CC_{249}$	0.74±0.08	0.41±0.09	1.15±0.10
$2002GH_{32}$[a]	0.85±0.07	0.91±0.05	1.75±0.08
$2002GJ_{32}$[a]	0.70±0.09	0.42±0.09	1.12±0.12
$2002KW_{14}$	1.11±0.06	0.91±0.04	2.02±0.06
$2002MS_4$	0.68±0.01	0.41±0.01	1.09±0.01

[a] Objects with colors in other published works: $V\text{–}R_{2000CN105} = 0.67\pm0.13$ (Peixinho et al. 2004); $B\text{–}R_{2002GH32} = 1.48\pm0.23$ and $B\text{–}R_{2002GJ32} = 1.50\pm0.19$ (Doressoundiram et al. 2005)

DATA ANALYSIS

Fraction Red versus Inclination

Using the enlarged dataset of 157 objects (increased both by the data from this work as well as other work submitted to the MBOSS database as of September 25, 2005), the fraction of red KBOs versus KBP inclination were plotted, including all classifications of KBOs in the dataset (see Table 5, Figure 6). The error bars on the fraction of red KBOs are calculated assuming a binomial distribution. These bins have approximately equal numbers (~26) of KBOs with colors in each bin. Two functions were fit to the data using least squares fitting methods: linear (dashed) and inverted exponential (dotted). The red cutoff was set at $B–R > 1.56$, the median of the entire sample. This color index was chosen following Doressoundiram et al. (2001), since $B–R$ not only maximizes the number of data points available, but is also a good spectral discriminator. The fraction of red is highest in the core and decreases steadily to ~50% near the edge of the core. It then remains near 50% red until it reaches the outer halo and decreases again, down to almost entirely neutral. However, there is a huge gap between 17 and 27 degrees, so it is difficult to determine the exact nature of that region. The next step is to refine this plot by breaking the objects up into dynamical populations.

TABLE 5: KBO STATISTICS, BINNED BY INCLINATION WITH RESPECT TO THE KUIPER BELT PLANE. NOTE THAT RED IS DEFINED AS $B–R > 1.56$

Bin (i_k)	Num KBOs	Num Red	Num Neutral	Frac. red
0° - 1.6°	91	23	3	0.88±0.06
1.6° - 3.6°	143	18	8	0.69±0.09
3.6° - 7.0°	83	14	12	0.54±0.10
7.0° - 13.3°	76	9	18	0.33±0.09
13.3° - 19.6°	64	12	14	0.46±0.10
19.6° - 35.0°	69	4	22	0.15±0.07

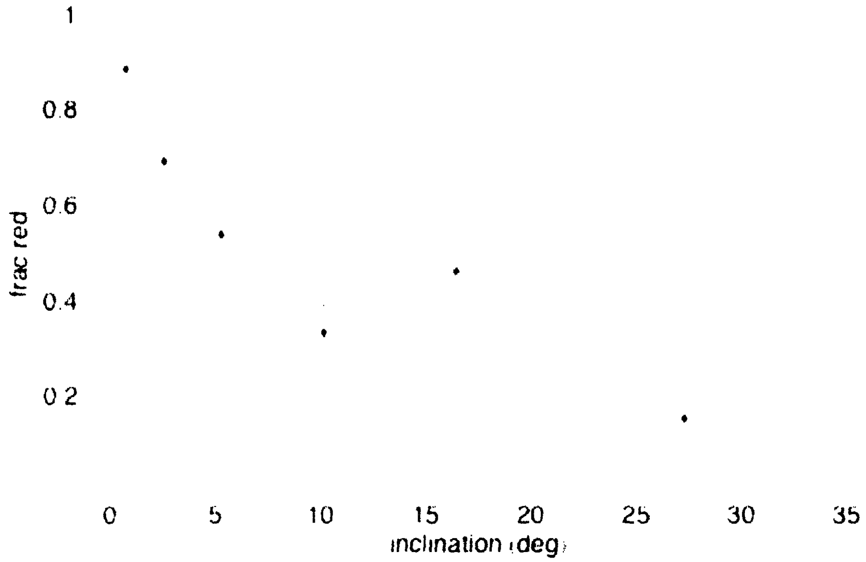

Figure 6: Fraction of red KBOs vs. KBP inclination for all classifications of KBOs. Red is determined as all objects with *B-R* > 1.56, the median of the entire sample. The bins contain approximately equal number of KBOs with colors. The dashed line, a linear regression, is expressed by fraction = (0.54±0.06)-(0.02±0.005)*(*i*-10.45). The dotted line, an inverse exponential, is expressed by fraction = (0.70±0.15)*e^(-0.15±0.09)+(0.24±0.12). The horizontal line at 4.6° represents the cutoff between core and halo as determined by the DES (Elliot et al. 2005).

Resonant Objects

Figure 7 shows the resonant objects plotted in several different KBP inclination bins (the same bins as in Table 1, Figure 6, and Figure 8). From these plots, we notice that the resonant objects do not show a correlation between color and inclination. Both of these datasets were fit with linear regressions. From these results, it is clear that the number of resonant objects as a whole show no color trends across inclination.

Figure 7: Fraction of red KBOs versus KBP inclination for the resonant KBOs. Red is determined as all objects with $B-R > 1.56$, the median of the entire sample. These two plots contain the same data, but have different inclination bins: The left figure has bins that contain an equal number of non-resonant KBOs with colors, while the right figure has bins that contain an equal number of KBOs with colors. The equation of the best-fit line through the figure on the left is fraction = $(0.46\pm0.04) - (0.004\pm0.004)*(i_K - 8.44)$. The equation of the best-fit line through the figure on the right is fraction = $(0.43\pm0.11) - (0.002\pm0.002)*(i_K - 8.49)$. The equations of both the lines clearly indicate that within these bin groupings, the fraction of resonant objects is approximately 50% red.

Additionally, while studying the origin of Pluto's orbit, Malhotra (1995) described the migration of the giant planets. As small objects in the outer solar system encountered Neptune, they were scattered either inward (where they came under the influence of Jupiter) or outward (where they either achieved Oort-cloud-like orbits or returned again to the vicinity of Neptune). Of the objects that returned, some came under the influence of Jupiter, while others again encountered Neptune. Given the bias that the inward scattered objects would be less likely to encounter Neptune again, Neptune's angular momentum increased, resulting in an increased orbital radius, causing it to "migrate" outwards. Malhotra (1995) concluded that Neptune swept up objects into resonances as it migrated outwards. Given these objects' evolutions, their compositions and environmental histories probably differ from that of the other KBOs. Based on Malhotra's conclusion, resonant objects were not included in this sample.

However, the Resonant objects show some interesting trends in and of themselves. Currently, the Resonant objects with measured colors are dominated by the Plutinos (those objects in a 3:2 resonance with Neptune), which span both red and neutral colors. By analyzing specific resonances, other color patterns emerge: objects in the 7:4 and 7:3 resonances are extremely red, while the 5:2 resonance contains almost entirely neutral objects (see Table 6). More data need to be gathered to avoid the pitfalls of small number statistics.

TABLE 6: STATISTICS FOR RESONANT OBJECTS DIVIDED INTO INDIVIDUAL RESONANCES

Class	Num objects	Median *B-R*	% Red
All	158[a]	1.564	50
Non-Res.	110	1.59	53.15
Resonant	47	1.509	42.55
4:3	1	1.857	100
3:2	30	1.449	43.33
5:3	1	1.637	100
7:4	4	1.995	100
2:1	4	1.536	50
7:3	1	1.927	100
5:2	6	1.333	16.67

[a] 158 objects were used in the "All" sample, although 157 objects were used for all other analysis. This discrepancy is the result of 1 object having the classification "ERR2LARGE." ERR2LARGE implies that the position of the object is not yet known well enough to determine its classification. This object was not included in any other analyses since it is as yet undetermined whether it is Resonant or not.

Non-Resonant Objects

Removing the Resonant objects, the fraction of red KBOs versus KBP inclination were re-plotted, using bins that have the same number of non-Resonant KBOs in each bin. There are 108 non-Resonant objects divided into 6 bins of 18 objects each. Table 7 shows the number of non-Resonant KBOs that are red and neutral in each bin. The number of red KBOs decreases as a function of inclination, with two plateaus in bins 2-3 and bins 5-6. The percentages drop quickly from 94% to 22% red, although the error bars on the last 5 bins are still large.

TABLE 7: NON-RESONANT KBO STATISTICS, BINNED BY INCLINATION WITH RESPECT TO THE KUIPER BELT PLANE. NOTE THAT RED IS DEFINED AS *B–R* > 1.56

Bin (i_k)	Num KBOs	Num Red	Num Neutral	Frac. red
0° - 1.2°	59	16	2	0.89±0.07
1.2° - 2.6°	118	14	4	0.78±0.10
2.6° - 8.3°	159	13	6	0.68±0.11
8.3° - 15.5°	78	8	10	0.44±0.12
15.5° - 23.2°	68	4	15	0.21±0.09
23.2° - 35.0°	44	4	14	0.22±0.10

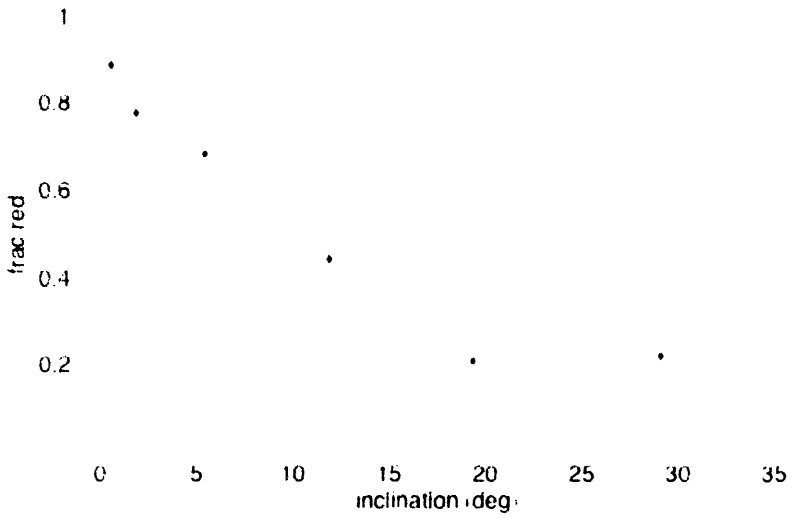

Figure 8: Fraction of red KBOs vs. KBP inclination for non-resonant of KBOs. Red is determined as all objects with *B–R* > 1.56, the median of the entire sample. The bins contain equal numbers of non-Resonant KBOs with colors. The dashed line, a linear regression, is expressed by fraction = (0.58±0.04)-(0.03±0.004)*(*i*-10.36). The dotted line, an inverse exponential, is expressed by fraction = (0.83±0.11)*e^(-0.081±0.03)+(0.01±0.13). The horizontal line at 4.6° represents the cutoff between core and halo as determined by the DES (2005).

Figure 8 plots the corresponding numbers in the table. This figure displays the same general decrease in the fraction of red KBOs as inclination increases, as seen in the all-KBO plot (Figure 6), but the initial decrease in fraction red begins at a much lower inclination and then the fraction decreases linearly to the far outer halo, where it levels off to almost entirely neutral (only 22% red) near 20 degrees.

DISCUSSION

Trujillo and Brown (2002) showed that there is an apparent linear correlation between KBO orbital inclination with respect to the ecliptic and *B–R* color. Moving out in inclination, objects become less red. Here, using almost 3 times as many objects and performing the analysis based on inclinations with respect to the Kuiper Belt plane, we note that the number of objects with *B–R* > 1.56 decreases with increasing inclination, leveling out near the transition from core to halo and in the outer halo. In fact, it appears that between these two plateaus, from 5 degrees to 20 degrees, the relationship between the fraction of red KBOs and inclination is linear. Also, the core is almost entirely red (peaking at 94% in the most-interior bin) while the outer halo is almost entirely neutral (down to 22%).

Colors of Kuiper Belt objects

The variations in the colors of KBOs are posited to be a reflection of their environments and represent different compositions or formation characteristics within the Kuiper Belt. Today, very little is irrefutably known about the composition of KBOs and exactly what clues their physical parameters will provide with respect to understanding the formation of the outer solar system. Characterizing these objects and understanding the differences between them will provide invaluable information about the physical and chemical processes that took place during the formation of our solar system.

Why Are KBO Colors Diverse?

The trends described above beg the question, 'Why are KBO colors diverse?' At the moment, there are two general schools of thought on this problem and the correct solution is unclear. One school is based on the idea that red implies unperturbed due to the "irradiation" crust. The objects that are not as perturbed have more time to get peacefully irradiated by cosmic rays and therefore appear redder. As objects undergo collisions or cometary outbursts, fresh ices from beneath the surface settle on the object and "rejuvenate" its neutral color. Another school believes that there are two distinct populations in the Kuiper Belt and that these two populations have inherent compositional differences resulting in the color diversity. Several groups have explored both these concepts.

The first to explore the concept of irradiated crusts being linked to color, Green et al. (1997) followed the path that extreme red colors are due to organic tholins created by cosmic radiation (Binzel 1992; Fink et al. 1992; Mueller et al. 1992; Davies et al. 1993). To become red, the surfaces are irradiated for 4.6×10^9 yrs by cosmic rays, resulting in the irradiation mantle. Collisions expose the fresh material beneath the surface (Luu and Jewitt 1996a). For the age of the solar system, there are ~10 impacts on a 100-km KBO. However, if this were the case, then there should be color correlations between semi-major axis (irradiation mantle) and eccentricity (collisions), which are not observed. In fact, Jewitt & Luu (2001) reject the resurfacing hypothesis as the primary coloring agent since no correlation is found between color and the difference between the average velocity and the reference velocity (the velocity of an object at the same semi-major axis, but 0° inclination and eccentricity).

When Gil-Hutton (2002) revisited the collisional resurfacing model, he accounted for superficial solar irradiation as well as the more substantial cosmic-ray irradiation and showed that this model could in fact account for the color diversity among KBOs. He described how a "thick" irradiation mantle could form, resulting in two possible collisional resurfacing regimes. In one case, very energetic collisions could reach the fresh ices beneath the thick mantle and rejuvenate the surface. In the other case, the "superficial" collisions would only resurface the KBO with a redder mantle. Doressoundiram et al. (2002) did find a correlation between mean excitation velocity and color, implying that space weathering or impact gardening may indeed be a factor in the color diversity. Stern (2002) confirmed the correlation between color and mean random-collision velocity, implying that the color diversity is in part explained by collisions, although he points out that there are still many unexplained aspects of this theory. Collisional resurfacing does play a role in the color diversity, but it is not the entire story.

Delsanti et al. (2004) reworked the collisional resurfacing model again, this time adding the neutralizing factor of "cometary outbursts." Here, gas outbursts re-cover the surface with non-irradiated dust, triggered either by collisions or produced spontaneously. Whether an outburst completely resurfaces the KBO depends on the objects size and heliocentric distance. This enhanced model still accounts for the color diversity of the KBOs and also accounts for the lack of rotational color effects, unlike the previous models. However, the relationship between color and inclination is still not predicted in this new model. In fact, for objects between 10-100km in radius, it suggests a correlation opposite to that observed. Delsanti et al. (2004) suggest that the average collisional energy, which is not accounted for in this model, could play a role in the disparity between model and observation. Assuming the collisional resurfacing hypothesis is right, objects with increasing inclination could be experiencing more collisions and cometary activity.

Colors of Kuiper Belt objects

Exploring the idea that color differences may result from inherently different groups of objects, Gomes (2003b) modeled two separate populations. The hot objects originated in the inner solar system and were perturbed by Neptune and Saturn. The cold objects originated in their present location of the Kuiper Belt and constitute a true primordial population. Under this model, the color-inclination correlation is then explained as the core/cold objects having formed differently from the halo/hot objects and therefore, having different colors. Figure 9, taken from Gomes' 2003 First Decadal Review of the Edgeworth-Kuiper Belt talk (Gomes 2003a), shows a cartoon of how these two populations would coexist.

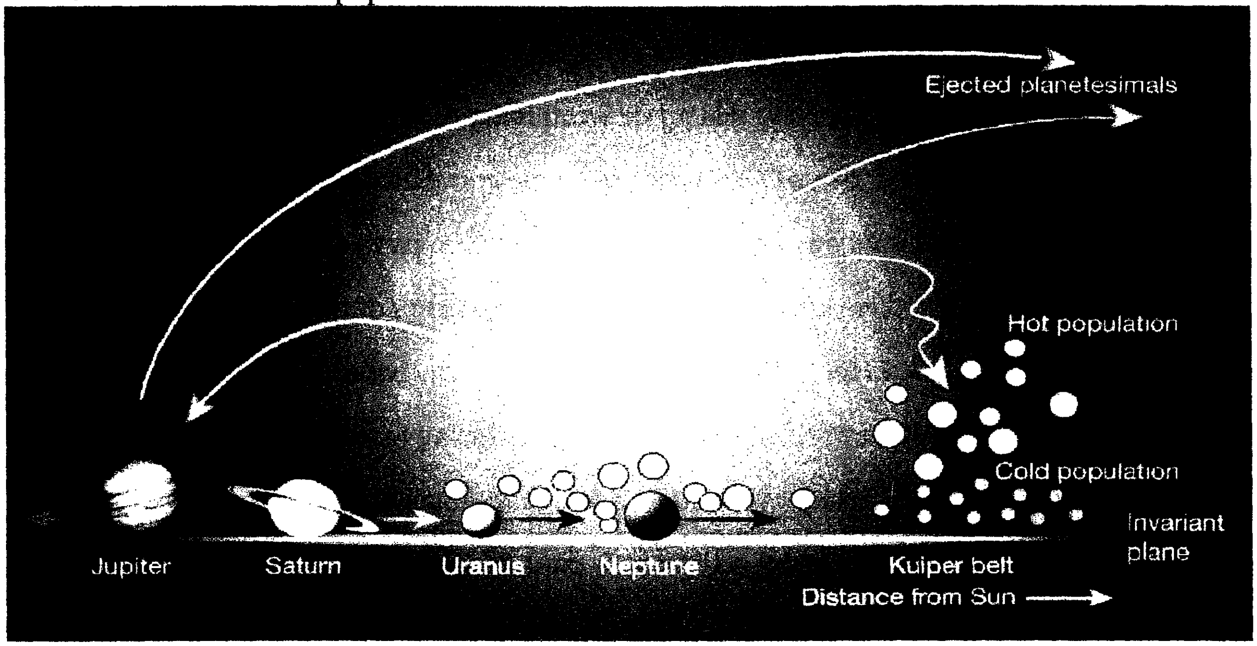

Figure 9: Possible solar system formation scenario resulting in two Kuiper Belt populations. As the outer planets migrated, they ejected some of the smaller inner bodies into the hot Kuiper Belt. The objects that form the cold Kuiper Belt formed there as a primordial population. Figure take from Gomes' 2003 talk at the First Decadal Review of the Edgeworth-Kuiper Belt in Antofagasta, Chile.

Levison & Morbidelli (2003) suggested that the cold population also formed closer to the Sun, but was captured in the 2:1 mean-motion resonance with Neptune while it migrated outward. When these primordial objects were finally deposited in their current locations, they maintained their low inclination orbits and thus remained cold. However, this model overestimates the values of the observed eccentricities, since migration would increase the eccentricity of their orbits. One potential resolution of this issue stems from a secular resonance in the 2:1 mean motion resonance. This resonance resulted in the eccentricities of the objects oscillating, accounting for the low eccentricities observed. However, Levison & Morbidelli (2003) did not perform the extensive modeling necessary to test this hypothesis.

CONCLUSIONS AND FUTURE WORK

This work confirms a trend between KBO colors and inclination: the fraction of red object decreases with increasing inclination. Based upon the idea that redder objects are less perturbed, the findings here imply that objects with lower inclinations are less likely to collide with other objects or undergo cometary outburst, allowing them to "peacefully" irradiate and become redder. Conversely, the objects that have higher inclinations collide more frequently and have more cometary outbursts. No matter what the process that affects these objects, the smooth transition implies that this process is biased with respect to inclination. Alternatively, the redness of the core and the neutrality of the outer halo support the idea of two distinct populations. The transition continues to be indicative of some process modifying the objects over inclination-space. It is most likely that the agent coloring these objects is a combination of both these ideas.

While this work has revealed interesting developments, more work is needed to improve the quality of these results. First, calculating new color transformations using data taken on both KBOs and standard stars in all Sloan and Johnson-Cousin filters will eliminate errors introduced by the color transformations. Second, using point-spread function (PSF) fitting instead of aperture correction can more accurately model the KBOs and standard stars, allowing inclusion of more of the light from the sources while decreasing the background contamination. Additionally, as noted above, the Resonant objects are not well sampled, but do show some possibly interesting trends. These trends should be investigated further in order to better understand the conditions that cause the color variations.

Here, 157 KBOs have *B–R* colors while there are more than 1000 observed KBOs. In order to more clearly understand the relationship between color and inclination, more data is required to reduce error bars and avoid the pitfalls of small number statistics.

REFERENCES

Barucci, M. A., A. Doressoundiram, D. Tholen, M. Fulchignoni, and M. Lazzarin 1999. Spectophotometric observations of Edgeorth-Kuiper belt objects. *Icarus* **142**, 476-481.

Barucci, M. A., M. Fulchignoni, M. Birlan, A. Doressoundiram, J. Romon, and H. Boehnhardt 2001. Analysis of Trans-Neptunian and Centaur colours: continuous trend or grouping? *Astron. & Astrophys.* **371**, 1150-1154.

Barucci, M. A., J. Romon, A. Doressoundiram, and D. J. Tholen 2000. Compositional Surface Diversity in the Trans-Neptunian Objects. *Astrophys. J.* **120**, 496-500.

Binzel, R. P. 1992. The optical spectrum of 5145 Pholus. *Icarus* **99**, 238-240.

Boehnhardt, H., G. P. Tozzi, K. Birkle, O. Hainaut, T. Sekiguchi, M. Vair, J. Watanabe, G. Rupprecht, and T. F. I. Team 2001. Visible and near-IR observations of transneptunian objects: Results from ESO and Calar Alto telescopes. *Astron. & Astrophys.* **378**, 653-667.

Brown, M. E. 2001. The inclination distribution of the Kuiper belt. *Astron. J.* **121**, 2804-2814.

Buie, M. W., R. L. Millis, L. H. Wasserman, J. L. Elliot, S. D. Kern, K. B. Clancy, E. I. Chiang, A. B. Jordan, K. J. Meech, R. M. Wagner, and D. E. Trilling 2003. Procedures, resources and selected results of the Deep Ecliptic Survey. *Earth, Moon, and Planets* **92**, 113-124.

Caldwell, J. A. R., A. W. J. Cousins, C. C. Ahlers, P. van Wamelen, and E. J. Maritz 1993. Statistical relations between the photometric colours of common types of stars in the UBV(RI)c, JHK and uvby systems. *SAAO Circulars* **15**,

Davies, J. K., S. Green, N. McBride, E. Muzzerall, D. J. Tholen, R. J. Whiteley, M. J. Foster, and J. K. Hillier 2000. Visible and Infrared Photometry of Fourteen Kuiper Belt Objects. *Icarus* **146**, 253-.

Davies, J. K., M. V. Sykes, and D. P. Cruikshank 1993. Near-infrared photometry and spectroscopy of the unusual minor planet 5145 pholus (1992 AD). *Icarus* **102**, 166-169.

Davis, L. 1987. Specifications for the Aperture Photometry Package.

Delsanti, A., O. Hainaut, E. Jourdeuil, K. J. Meech, H. Boehnhardt, and L. Barrera 2004. Simultaneous visible-near IR photometric study of Kuiper belt object surfaces with the ESO/Very Large Telescopes. *Astron. & Astrophys.* **417**, 1145-1158.

Doressoundiram, A., M. A. Barucci, and J. Romon 2001. Multicolor Photometry of Trans-neptunian Objects. *Icarus* **154**, 277-286.

Doressoundiram, A., N. Peixinho, C. De Bergh, S. Fornasier, P. Thebault, M. A. Barucci, and C. Veillet 2002. The Color Distribution in the Edgeworth-Kuiper Belt. *Astron. J.* **124**, 2279-2296.

Doressoundiram, A., N. Peixinho, C. Doucet, O. Mousis, M. A. Barucci, J. M. Petit, and C. Veillet 2005. The Meudon Multicolor Survey (2MS) of Centaurs and trans-neptunian objects: extended dataset and status on the correlations reported. *Icarus* **174**, 90-104.

Edgeworth, K. E. 1949. The origin and evolution of the solar system. *Mon. Not. Roy. Astron. Soc.* **109**, 600-609.

Elliot, J. L., S. D. Kern, K. B. Clancy, A. A. S. Gulbis, R. L. Millis, M. W. Buie, L. H. Wasserman, E. I. Chiang, A. B. Jordan, D. E. Trilling, and K. J. Meech 2005. The Deep Ecliptic Survey: A search for Kuiper belt objects and Centaurs. II. Dynamical classification, the Kuiper belt plane, and the core population. *Astron. J.* **129**, 1117-1162.

Fink, U., M. Hoffmann, W. Grundy, M. D. Hicks, and W. Sears 1992. The steep red spectrum of 1992 AD - an asteroid covered with organic material? *Icarus* **97**, 145-149.

Gil-Hutton, R. 2002. Color diversity among Kuiper belt objects: The collisional resurfacing model revisited. *Planet. & Space Sci.* **50**, 57-62.

Gomes, R. S. 2003a.

Gomes, R. S. 2003b. The common origin of the high inclination TNOs. *Earth, Moon, and Planets* **92**, 29-42.

Green, S. F., N. McBride, D. R. O'Ceallaigh, A. Fitzsimmons, I. P. Williams, and M. J. Irwin 1997. Surface reflectance properties of distant solar system bodies. *Mon. Not. Roy. Astron. Soc.* **290**, 186-192.

Gulbis, A. A. S., J. L. Elliot, and J. F. Kane 2006. The color of the Kuiper belt core. *Icarus* (in press).

Hainaut, O., and A. Delsanti 2002. Colors of minor bodies in the outer solar system. *Astron. & Astrophys.* **389**, 641-664.

Howell, S. B. 1989. Two-Dimensional Aperture Photometry:Signal-To-Noise ratio of Point-Source Observations and Optimal Data-Extraction Techniques. *Publ. Astron. Soc. Pacific* **101**, 616-622.

Jewitt, D. C., and J. X. Luu 1993. Discovery of the candidate Kuiper belt object 1992 QB1. *Nature* **362**, 730-732.

Jewitt, D. C., and J. X. Luu 1998. Optical-infrared spectral diversity in the Kuiper Belt. *Astron. J.* **115**, 1667-1670.

Jewitt, D. C., and J. X. Luu 2001. Colors and spectra of Kuiper belt objects. *Astron. J.* **122**, 2099-2114.

Kern, S. D. 2005. *A study of Binary Kuiper Belt objects.* PhD Thesis, Earth, Atmospheric and Planetary Sciences, MIT, Cambridge.

Kuiper, G. P. 1951. On the origin of the solar system. In *Astrophysics* (J. A. Hynek, Ed.), pp. 357-424. McGraw Hill, New York.

Leonard, F. C. 1930. The new planet Pluto. *Astronomical Society of the Pacific Leaflet* **1**, 121.

Levison, H. F., and A. Morbidelli 2003. The formation of the Kuiper belt by the outward transportation of bodies during Neptune's migration. *Nature* **426**, 419-421.

Levison, H. F., and S. A. Stern 2001. On the size dependence of the inclination distribution of the main Kuiper Belt. *Astron. J.* **121**, 1730-1735.

Luu, J. X., and D. C. Jewitt 1996a. Color diversity among the Centaurs and Kuiper Belt objects. *Astron. J.* **112**, 2310-2318.

Luu, J. X., and D. C. Jewitt 1996b. The Kuiper Belt. *Scientific American* **274**, 32-38.

Malhotra, R. 1995. The origin of Pluto's orbit: Implications for the solar system beyond Neptune. *Astron. J.* **110**, 420-429.

Millis, R. L., M. W. Buie, L. H. Wasserman, J. L. Elliot, S. D. Kern, and R. M. Wagner 2002. The Deep Ecliptic Survey: A search for Kuiper Belt objects and Centaurs I. Description of methods and initial results. *Astron. J.* **123**, 2083-2109.

Morbidelli, A., M. E. Brown, and H. F. Levison 2003. The Kuiper Belt and its Primordial Sculpting. *Earth, Moon, and Planets* **92**, 1-27.

Mueller, B. E. A., D. J. Tholen, W. K. Hartman, and D. P. Cruikshank 1992. Extraordinary colors of asteroidal object (5145) 1992 AD. *Icarus* **97**, 150-154.

Murray, C. D., and S. F. Dermott 1999. *Solar System Dynamics.* Cambridge University Press, Cambridge.

Osip, D. J., D. M. Phillips, R. Bernstein, G. Burley, A. Dressler, J. L. Elliot, E. Persson, S. A. Shectman, and I. Thompson 2004. First-generation instruments for the Magellan telescopes: characteristics, operation, and performance. In *Ground-based Instrumentation for Astronomy* (A. F. M. Moorwood and I. Masanori, Ed.), pp. 49-59.

Peixinho, N., H. Boehnhardt, I. N. Belskaya, A. Doressoundiram, M. A. Barucci, and A. Delsanti 2004. ESO large program on Centaurs and TNOs: visible colors - final results. *Icarus* **170**, 153-166.

Romon-Martin, J. 1999. Master's thesis. *Universite Paris XI*

Smith, J. A., D. L. Tucker, S. Kent, M. W. Richmond, M. Fukugita, T. Ichikawa, S. Ichikawa, A. M. Jorgensen, A. Uomoto, J. E. Gunn, M. Hamabe, M. Watanabe, A. Tolea, A. A. Henden, J. Annis, J. R. Pier, T. A. McKay, J. Brinkmann, B. Chen, J. Holtzman, K. Shimasaku, and D. G. York 2002. The u' g' r' i' z' standard-star system. *Astron. J.* **123**, 2121-2144.

Stern, S. A. 2002. Evidence for a collisional mechanism affecting Kuiper Belt object colors. *Astron. J.* **124**, 2297-2299.

Stetson, P. B. 1987. DAOPHOT: A computer program for crowded-field stellar photometry. *Publ. Astron. Soc. Pacific* **99**, 191 - 222.

Tegler, S. C., and W. Romanishin 1998. Two distinct populations of Kuiper-belt objects. *Nature* **392**, 49-50.

Tegler, S. C., and W. Romanishin 2000. Extremely red Kuiper belt objects in near-circular orbits beyond 40 AU. *Nature* **407**, 979-980.

Tegler, S. C., W. Romanishin, and G. J. Consolmagno 2003. Color patterns in the Kuiper belt: A possible primordial origin. *Astrophys. J.* **599**, L49-L52.

Trujillo, C. A., and M. E. Brown 2002. A correlation between inclination and color in the classical Kuiper belt. *Astrophys. J. Lett.* **566**, L125-L128.

Young, A. T. 1974. Other Components in Photometric Systems. In *Methods of Experimental Physics: Astrophysics* (N. Carleton, Ed.), pp. 101. Academic Press, New York.